Coherent Multi-Transducer Ultrasound Imaging

Laura Peralta, Alberto Gomez, Ying Luan, Baehyung Kim, Joseph V Hajnal and Robert J Eckersley

***Abstract*—This work extends the effective aperture size by coherently compounding the received radio frequency data from multiple transducers. As a result, it is possible to obtain an improved image, with enhanced resolution, an extended field of view and at high acquisition frame rates. A framework is developed in which an ultrasound imaging system consisting of N synchronized matrix arrays, each with partly shared field of view, take turns to transmit plane waves. Only one individual transducer transmits at each time while all N transducers simultaneously receive. The subwavelength localization accuracy required to combine information from multiple transducers is achieved without the use of any external tracking device. The method developed in this study is based on the study of the backscattered echoes received by the same transducer and resulting from a targeted scatterer point in the medium insonated by the multiple ultrasound probes of the system. The current transducer locations along with the speed of sound in the medium are deduced by optimizing the cross-correlation between these echoes. The method is demonstrated experimentally in 2-D for 2 linear arrays using point targets and anechoic lesion phantoms. A first demonstration of a free-hand experiment is also shown. Results demonstrate that the coherent multi-transducer ultrasound imaging method has the potential to improve ultrasound image quality, improving resolution and target detectability. Compared with coherent plane wave compounding using a single probe, lateral resolution improved from 1.56 mm to 0.71 mm in the coherent multi-transducer imaging method without acquisition frame rate sacrifice (acquisition frame rate 5350 Hz).**

***Index Terms*—Mulit-probe, Image resolution, Large aperture, Plane Wave, Ultrasound imaging**

I. Introduction

ULTRASOUND is a widely used clinical imaging tool and its advantages in terms of portability, safety and low cost over other medical imaging modalities are well known. However, there are still some main challenges that remain in ultrasound imaging and limit the usability of conventional ultrasound systems for certain applications. Conventional ultrasound images may be difficult to assess because of the restricted field of view (FoV) that often prevents the acquisition of the entire object of interest, the limited resolution and the view-dependent artefacts. These challenges are particularly present when imaging at larger depths in abdominal or fetal imaging applications [1], [2] and inherent to the small aperture transducers used clinically. To increase the FoV, multiple images, acquired mechanically moving the probe [3] or by different probes [4], can be incoherently compounding together in the lateral direction using image registration. However, the resolution of the resulting image is not improved by such approaches. Alternatively, increased resolution may be achieved by advanced beamforming. For example, minimum variance adaptive beamforming has been shown to improve ultrasound image resolution compared with the standard delay-and-sum method [5]. Finally, the relatively slow frame rate (about 20 to 40 frames per second), determined by the number of scan lines and the imaging depth, restricts the use of conventional ultrasound systems for certain applications, such as real-time 3-D imaging, shear wave elastography or cardiac cycle monitoring [6]. Although adaptive beamforming methods in combination with multi-line transmission and acquisition approaches can increase the frame rate of focal linear scanning [5], [7], this frame rate is still not enough for many applications. Methods such as coherent plane wave compounding [6], [8] and synthetic aperture [9], [10] allow generation of images similar in quality to conventional focused-mode images but acquired with frame rates typically in the kHz range.

A direct way to enhance resolution and imaging performance is by extending the aperture of the imaging system [11]. Recently, the improvements of a wider coherent aperture have been shown in synthetic aperture ultrasound imaging [12], [13], where an extended aperture was obtained by mechanically moving the ultrasound transducer. An external tracker was used to identify the relative position and orientation of the ultrasound images which were then merged together into a final image. However, noise in the tracking system and calibration errors are propagated to coherent image reconstruction causing image degradation. The subwavelength localization accuracy required to merge information from multiple transducers is challenging to achieve in conventional ultrasound calibration. Resolution will suffer from motion artefacts, tissue deformation or tissue aberration, which worsen with increased effective aperture size [14], [15]. For practical implementation, a more accurate calibration technique is required [13], [16]. In addition, the viability of the technique *in-vivo* is limited by the long acquisition times ($>$15 minutes per image) that may also contribute to the break down of the coherent aperture [12].

In addition to technical limitations, in clinical practice the aperture size is limited not only by the complexity of the system and its high cost but also by the low flexibility that a large probe may have for different situations. Clinical probes must be controlled and moved by a physician to adapt to contours and shapes of the human anatomy. The physical transducer size is then a compromise between cost, ergonomics and image performance. Fabrication of flexible probes that can adapt to the body has not been successfully implemented because the sub-wavelength localization of transducer elements is required for accurate coherent image formation, and this is currently infeasible with external trackers as discussed before. However,

L. Peralta, A. Gomez, B. Kim, Y. Luan, J. Hajnal and R. Eckersley are with the Department of Biomedical Engineering, School of Biomedical Engineering & Imaging Sciences, King's College London, King's Health Partners, St Thomas' Hospital, London, SE1 7EH, United Kingdom (e-mail: laura.peralta-pereira@kcl.ac.uk).

Y. Luan is with GE Healthcare.

B. Kim is with Ultrasound Research Laboratory, Physiology and Biomedical Engineering, Mayo Clinic College of Medicine, Rochester, USA.

exploiting the correlation between the received signals on different physical apertures may allow the relative positions of the transducer elements to be determined with sufficient accuracy. To demonstrate this concept, this paper describes coherent combination of conventional array transducers using a plane wave (PW) imaging approach, in order to provide a significantly extended aperture. The motivation of this work is to demonstrate the potential of the approach and provide a proof-of-concept as an initial step towards large array imaging using independently placed transducers to form non-continuous extended apertures. The novelty of this work lies in the use of the mutual information available in the signals received by the individual transducers that form the extended array to provide precise relative positioning information so that they might be used as one coherent whole. A unique aspect of this approach is that it does not require an external tracking system to achieve accurate localization. Instead, the coherence in the backscattered echoes resulting from point-like scatterers in the medium is used to determine the relative position of multiple transducers with respect to a single transducer.

This work is organized as follows. The theory is presented in a general 3-D framework for matrix arrays in Section II. The principles of plane wave imaging are summarized in Section II-A along with the nomenclature used to beamform data acquired by multiple transducers. Section II-B describes the method for accurate calculation of the spatial location of the different transducers. Then the method is experimentally validated in 2-D using two identical linear arrays. Experimental methods are described in Section III. The corresponding results, using the multi-transducer system, are presented in Section IV. To evaluate the potential gains in resolution and image contrast provided through our approach, all results are compared to coherent PW compounding imaging with one single transducer and the incoherently compounded image obtained with the multiple transducers. Finally, the implications of this work, including the limitations, are discussed in Section V. The study is concluded is Section VI.

II. Theory

Ultrasound image quality improves by reducing the F-number, which represents the ratio of the focusing depth to the aperture size. Expanding the aperture is a direct way to improve imaging performance. Preliminary in silico and phantom works suggest that different transducers can be coherently combined, significantly increasing the aperture size of the system and improving image resolution [17], [18].

In the proposed coherent multi-transducer method, a single transducer is used for each transmission to produce a PW that insonates an entire FoV of the transmit transducer. The resulting echoes scattered from the medium are recorded using all the transducers that form the system. The sequence is continued by transmitting from each individual transducer in turn. Knowing the location of each transducer and taking into account the full transmit and receive path lengths, coherent summation of the radio frequency (RF) data from multiple transducers can be used to form a larger aperture and get an image, following the same approach as in PW imaging [6].

A. Multi-transducer notation and beamforming

A 3-D framework consisting of N identical matrix arrays (T_i, $i = 1, \ldots, N$) that are freely placed in space and have a partly shared FoV is considered. The transducers are otherwise at arbitrary positions. All transducers are synchronized (i.e. trigger and sampling times in both transmit and receive mode are the same), and take turns to transmit a plane wave. Every transmitted wave is received by all transducers, including the transmit one. Thus, a single plane wave shot will yield N RF datasets, one for each receiving transducer.

The framework is described using the following nomenclature. Points are noted in upper case letters (e.g. P), vectors representing relative positions are represented in bold lowercase (e.g. $\mathbf{r}$), unit vectors are noted with a "hat" (e.g. $\hat{x}$) and matrices are written in bold uppercase (e.g. $\mathbf{R}$). Index convention is to use i for the transmitting transducer, j for the receiving transducer, h for transducer elements, and k for scatterers. Other indices are described when used.

The set-up is illustrated in Fig. 1 for the simplest case of 2 transducers. The resulting image and all transducer coordinates are defined in a world coordinate system arbitrarily located in space. The superscript ^{i} denotes when the transducer's local coordinates are used. The position and orientation of a transducer T_i is represented by the origin O_i, defined at the center of the transducer surface, and the local axes $\{\hat{x}_i, \hat{y}_i, \hat{z}_i\}$, with the $\hat{z}_i$ direction orthogonal to the transducer surface and directed away from transducer i. A plane wave transmitted by transducer T_i is defined by the plane $\mathcal{P}_a^i$, which can be characterized through the normal to the plane $\hat{n}_i$ and the origin O_i. The RF data received by transducer j on element h at time t is noted $T_iR_j(h, t)$.

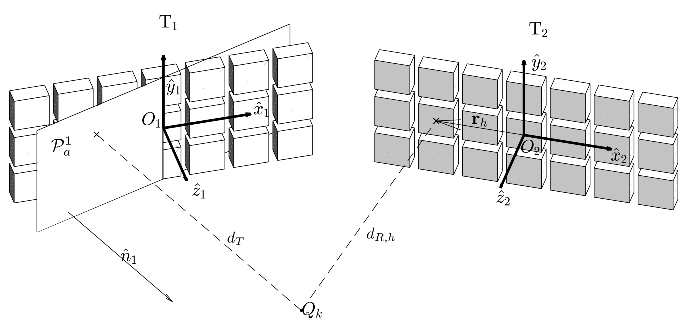

Fig. 1. Geometric representation of the multi-transducer beamforming scheme. In this example, transducer T_1 transmits a plane wave at certain angle defined by $\mathcal{P}_a^1$ and T_2 receives the echo scattered from Q_k on element h.

Using the above notation, PW imaging beamforming [6] can be extended to the present multi-transducer set-up. Assuming that transducer T_i transmits a plane wave at certain angle defined by $\mathcal{P}_a^i$, the image point to be beamformed located at Q_k can be computed from the echoes received at transducer T_j as:

$$s_{i,j}(Q_k; \mathcal{P}_a^i) = \sum_{h=1}^{H} T_iR_j\left(h, t_{i,j,h}(Q_k; \mathcal{P}_a^i)\right) = \sum_{h=1}^{H} T_iR_j\left(h, \frac{D_{i,j,h}(Q_k; \mathcal{P}_a^i)}{c}\right) \tag{1}$$

where H is the total number of elements in the array, c is the speed of sound of the medium, and D is the distance travelled by the wave, which can be split into the transmit and the receive distances:

$$D_{i,j,h}(Q_k; \mathcal{P}_a^i) = d_T(Q_k, \mathcal{P}_a^i) + d_{R,h}(Q_k, O_j + \mathbf{r}_h) \quad (2)$$

with d_T measuring the distance between a point and a plane (transmit distance), and $d_{R,h}$ being the distance between a point and the receive element (receive distance). These distances can be computed as follows:

$$d_T(Q_k, \mathcal{P}_a^i) = |(Q_k - O_i) \cdot \hat{n}_i| = |(Q_k - O_i) \cdot (\mathbf{R}_i \hat{n}_i^i)| \quad (3)$$

and

$$\begin{aligned} & d_{R,h}(Q_k, O_j + \mathbf{r}_h) = \\ & \|Q_k - (O_j + \mathbf{r}_h)\| = \|Q_k - (O_j + \mathbf{R}_j \mathbf{r}_h^j)\| \end{aligned} \quad (4)$$

where $\|\|$ is the usual Euclidean distance, and $\mathbf{R}_i = [\hat{x}_i \ \hat{y}_i \ \hat{z}_i]$ is a 3×3 matrix parameterized through three rotation angles, $\boldsymbol{\phi}_i = \{\phi_x, \phi_y, \phi_z\}_i$, that together with the offset O_i characterize the position and orientation of transducer T_i with 6 parameters [19].

With the total distances computed, equation (1) can be evaluated for each pair of transmit-receive transducers, and the total beamformed image $S(Q_k)$ can be obtained by coherently adding the individually beamformed images:

$$S(Q_k; \mathcal{P}_a) = \sum_{i=1}^{N} \sum_{j=1}^{N} s_{i,j}(Q_k; \mathcal{P}_a^i) \quad (5)$$

In the same vein, assuming that the location of the multiple transducers of the system is known over the acquisition time and the medium of interest do not move, several plane waves transmitted at different angles, $a = 1, \ldots, A$, may be coherently combined as well to generate an image,

$$S(Q_k; \mathcal{P}_A) = \sum_{i=1}^{N} \sum_{j=1}^{N} \sum_{a=1}^{A} s_{i,j}(Q_k; \mathcal{P}_a^i) \quad (6)$$

B. Calculation of the transducer locations

In order to carry out the coherent multi-transducer compounding described in the previous section, the position and orientation of each imaging transducer (defined by O_i and $\boldsymbol{\phi}_i$) are required. This then allows computation of the travel time of the transmitted wave to any receive transducer. This section describes a method to accurately calculate these positions by exploiting the consistency of received RF data when signals are received from the same medium insonated by different transducers.

A medium with K point scatterers located at positions Q_k, $k = 1, \ldots, K$ is considered. It is assumed that the speed of sound is constant and all transducers are identical (implications of these assumptions are discussed later in Section V). The following transmit sequence is considered: a single plane wave is transmitted by each probe in an alternating sequence, i.e. only one probe transmits at each time while all probes receive, including the transmit one. Since the use of plane waves enables a high transmit rate, it can be assumed that the system remains still during consecutive acquisitions. Then, the wavefields resulting from the same point scatterer and received by the same transducer T_j, from consecutive transmissions by all transducers $T_{i=1,\cdots,N}$, must be correlated or have spatial covariance [20]. Specifically, considering only the RF data received by transducer T_j (i.e. $T_{i=1,\cdots,N} R_j$), for each element h, any timing difference between them is the transmit time (receive time is equal since the receive transducer is the same). The signals received by element h will be correlated once the difference in transmit time is compensated. The proposed method consists of finding the optimal parameters for which the time correlation between the received RF datasets sharing the same receive transducer is maximum for K scatterers in the common FoV. Those parameters define the total reception time corresponding to each point scatterer Q_k, and are:

$$\theta = \{\mathcal{P}_a^1, ..., \mathcal{P}_a^N, c, Q_1, \ldots, Q_K, \boldsymbol{\phi}_1, O_1, \ldots, \boldsymbol{\phi}_N, O_N\} \quad (7)$$

Note that, in practice the angle of the transmitted plane wave is known and then the unknown parameters to optimize are the speed of sound and the locations of the scatterers and probes. In addition, since the parameters that define transducer locations in space depend on the definition of the world coordinate system, the vector of unknown parameters can be reduced by defining the world coordinate system the same as the local coordinate system of one of the receiver transducers, e.g. T_i ($\boldsymbol{\phi}_i = \{0, 0, 0\},\ O_i = [0, 0, 0]$).

Being T the time pulse length of the transmitted pulse, the envelope of the signal transmitted by transducer T_i backscattered by the scatterer Q_k and received by transducer T_j, i.e. $T_i R_j(h, t_{i,j,h}(Q_k; \mathcal{P}_a^i) + T)$ can be calculated as,

$$\begin{aligned} E_{(i,j,h,k;a)}[T] = E\{T_i R_j(h, t_{i,j,h}(Q_k; \mathcal{P}_a^i) + T)\} = \\ \big[T_i R_j(h, t_{i,j,h}(Q_k; \mathcal{P}_a^i) + T)^2 + \\ \mathcal{H}\{T_i R_j(h, t_{i,j,h}(Q_k; \mathcal{P}_a^i) + T)\}^2\big]^{1/2} \end{aligned} \quad (8)$$

where $\mathcal{H}$ is the Hilbert transform and to simplify the envelope of the signal is noted as $E_{(i,j,h,k;a)}[T]$.

Then, the similarity between signals received by the same element h of transducer T_j can be computed using equation (9), where NCC is the normalized crossed correlation.

Finally, the total similarity, $\chi_{j,k}$, between RF data received by the same transducer j can be calculated taking into account all the elements as,

$$\begin{aligned} \chi_{j,k}(\theta) = \sum_{i}^{N} \sum_{h}^{H} \mathrm{NCC}(E_{(i,j,h,k;a)}[T], \\ E_{(j,j,h,k;a)}[T]) W_{i,k,j,h}(\theta) W_{j,k,j,h}(\theta) \end{aligned} \quad (10)$$

where $W_{i,k,j,h}$ is defined as,

$$\begin{aligned} W_{i,k,j,h}(\theta) = \frac{1}{2} + \frac{1}{2H} \sum_{h_b \neq h}^{H} \mathrm{NCC}(T_i R_j(h, t_{i,j,h}(Q_k; \mathcal{P}_a^i) + T), \\ T_i R_j(h_b, t_{i,j,h}(Q_k; \mathcal{P}_a^i) + T)) \\ \text{with } h, h_b \in [1, \ldots, H] \end{aligned} \quad (11)$$

The function $W_{i,k,j,h}$ is a weighting factor proportional to the degree of coherence between pulses received across the

$$\textsc{ncc}(E_{(i,j,h,k;a)}[T], E_{(j,j,h,k;a)}[T]) = \frac{\sum_{\tau=0}^{T}(E_{(i,j,h,k;a)}[\tau] - \overline{E}_{(i,j,h,k;a)}[\tau])(E_{(j,j,h,k;a)}[\tau] - \overline{E}_{(j,j,h,k;a)}[\tau])}{\left[\sum_{\tau=0}^{T}(E_{(i,j,h,k;a)}[\tau] - \overline{E}_{(i,j,h,k;a)}[\tau])^2 \sum_{\tau=0}^{T}(E_{(j,j,h,k;a)}[\tau] - \overline{E}_{(j,j,h,k;a)}[\tau])^2\right]^{1/2}} \quad (9)$$

individual elements of a single transducer, i.e. how well each signal correlates with those from the rest of the elements of the same transducer.

Finally, summing over all receiving transducers of the system and scatterers yields the cost function:

$$\chi(\theta) = \sum_{j}^{N}\sum_{k}^{K}\chi_{j,k}(\theta) \quad (12)$$

Then, the optimal parameters $\bar{\theta}$, which include the relative position and orientation of all involved transducers, the speed of sound, and the position of the point scatterers can be found by a search algorithm that maximizes the cost function χ,

$$\bar{\theta} = \arg\max_{\theta}\chi(\theta) \quad (13)$$

Equation (13) can be maximized by using gradient-based optimization methods [21].

Knowing the relative position of the different transducers of the system, the RF data can be beamformed using equation (5). Note that, the world coordinate system where the multi-transducer image is reconstructed may be defined arbitrarily in space. A world coordinate system defined at the center of the total aperture of the system will lead to a more conventional point spread function (PSF), in which the best possible resolution is aligned with the lateral direction (x-axis) of the image.

C. Intuition and Uniqueness of solution

In a homogeneous medium with K point scatterers, the corresponding one-way geometric delay profile is a unique function of the target and array geometry and sound speed. Assuming a constant speed of sound in the medium, it is well known that the position of a point scatterer and the speed of sound can be estimated solely from the delays in the RF echo data recorded on individual elements of the receiver array [22], [23].

Given the position of a number of point scatterers and with the assumption of a uniform speed of sound, the relative locations of the receivers and transmitters that form the imaging system can be calculated in similar way to trilateration positioning problems [24]. To localize a point, trilateration uses the location of at least three reference points (two points in 2-D) and the distance between them and the point to be localized. In 2-D geometry, it is known that if a point lies on two circles, then the circle centers and the two radii provide sufficient information to narrow the possible locations down to two. In 3-D geometry, when it is known that a point lies on the surfaces of three spheres, then the centers of the three spheres along with their radii provide sufficient information to narrow the possible locations down to no more than two. In both cases, 2-D and 3-D, additional information may narrow the possibilities down to one unique location.

In the context of the multi-probe system presented in this work. Once the relative position between a scatterer and the transducer T_1 are known, it is possible to estimate the distance between the scatterer and the second transducer T_2 through comparison of the RF data received by T_1, i.e., T_1R_1 and T_2R_1. Each additional point scatterer detected determines a sphere of center $Q_k = (x_k, y_k, z_k)$ and radius $d_T(Q_k; \mathcal{P}_a^{T_2})$. The location of transducer T_2 is determined relative to T_1 by one of the two external tangent planes common to three spheres defined by three different point scatterers. The direct RF echo data received by transducer T_2 i.e. T_2R_2 and T_1R_2 then provides the extra information required to determine the unique solution. In 2-D geometry two point scatterers provide the information required to solve this trilateration problem.

III. Methods

The method was tested experimentally using 2 identical linear arrays having a partly shared FoV of an ultrasound phantom with both located on the same plane ($y = 0$). In this 2-D framework, the elevation dimension is removed from the problem and then the parameters that define the position and orientation of the transducers are reduced to one rotation angle $\{\phi\}$ and one 2-D translation O_j [19]. The experimental sequence starts with transducer 1 transmitting a plane wave into the region of interest (in the common FOV of transducer 1 and 2). Then, the backscattered ultrasound field is received by both transducers of the system (T_1R_1 and T_1R_2). This sequence is repeated but transmitting with transducer 2 and acquiring the backscattered echoes with both transducers, T_2R_1 and T_2R_2. Using this sequence, two different kind of experiments were carried out to validate the technique, a static configuration and a free-hand demonstration.

A. Experimental Setup

The experimental setup was composed of two synchronized 256-channel Ultrasound Advanced Open Platform (ULA-OP 256) systems (MSD Lab, University of Florence, Italy) [25]. Each ULA-OP 256 system was used to drive an ultrasonic linear array made of 144 piezoelectric elements with a 6 dB bandwidth ranging from 2 MHz to 7.5 MHz (imaging transducer LA332, Esaote, Firenze, Italy).

Before acquisition, probes were carefully aligned in the same elevational plane using a precision mechanical mount. Each probe was held by a 3-D printed shell structure that was connected to a double-tilt and rotation stage and then mounted on a xyz translation and rotation stage (Thorlabs, USA). Fig. 2 shows an annotated photograph of this setup. The imaging

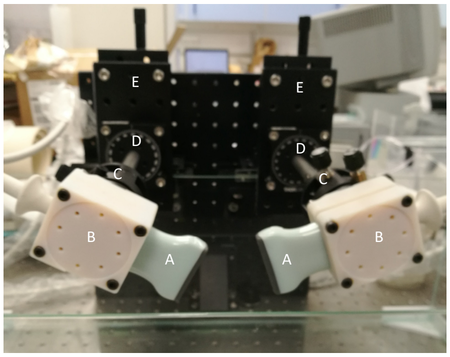

Fig. 2. Precision mechanical setup. Components are labeled with letters. (A) Linear array. (B) 3-D printed probe holder. (C) Double-tilt and rotation stage. (D) Rotation stage. (E) xyz translation stage.

plane of both transducers $(y = 0)$ was that defined by two parallel wires immersed in the water tank.

B. Phantom

Two different ultrasound phantoms were used to experimentally validate the method and characterize resolution and contrast. The first phantom was a custom-made wire target phantom (200-μm diameter) submersed in distilled water. Fig. 3 shows a schematic view of this experimental setup.

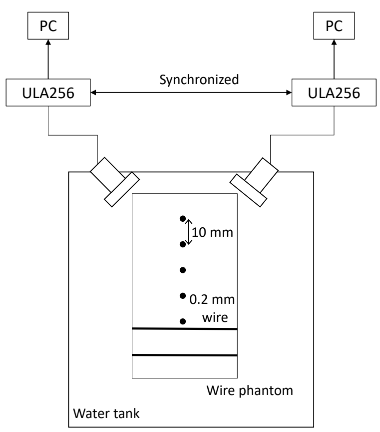

Fig. 3. Experimental setup for coherent multi-transducer ultrasound imaging.

For measurement of contrast, an anechoic lesion phantom was produced. It was formed in a rectangular polypropylene mould of dimensions 13.5 cm x 10.2 cm x 18.5 cm. Two parallel walls of the mould (section 13.5 cm x 18.5 cm) were drilled to create a series of 3 holes in a line spaced $\sim$ 10 mm apart. Three nylon wires (200-μm diameter) were passed through the holes and fixed. In line with these, a single cylindrical stainless steel bar (12.7 mm diameter, 102 mm) was also postioned (for later removal) to form the anechoic lesion.

Then, 1200 mL deionized water was mixed with 28 g of agar until dissolved. The mixture was heated in a microwave oven up to 90^o (boiling point of agar is 85^o). When the solution reached the boiling point, it was removed from the oven and allowed to cool at room temperature while being stirred using a magnetic stirrer. When the temperature reached 50^o, 50 g of graphite were added without stopping stirring. The solution was then poured into the rectangular mould described above.

After room temperature was reached, the solution in mould was allowed to settle down in the fridge for at least 12h. Then the sample was carefully removed from the mould, keeping the wires and the bar embedded. In a final step, the stainless steel bar was removed from the sample. The resulting hole was filled with a similar agar mixture, except without graphite to make the anechoic lesion.

During the experiments, the phantom was placed in a water tank at room temperature and positioned so that all wires and the anechoic region were in the common FoV of the 2 transducers.

C. Pulse sequencing and experimental protocol

Two different kind of experiments were carried out. First, a stationary acquisition in which both probes were mounted and fixed in the precision mechanical setup described above. Resolution and contrast were measured in these conditions using the two ultrasound phantoms described above. The second experiment consisted of a free-hand demonstration. In this case, both probes were held and controlled by an operator. The transducer movements were carefully restricted to the same elevational plane, i.e. $y = 0$ and to keep two common targets in the shared FoV. To facilitate the alignment of the probes, the operator kept them in contact and parallel to the wall of the water tank. Data was acquired on the wire-phantom.

PW imaging was used for all the experiments. Plane waves were transmitted from the 144 elements of each probe at 3 MHz with a pulse repetition frequency (PRF) equal to 4000 Hz and RF data were acquired at a sampling frequency of 39 MHz. No apodization was applied either on transmission or reception. The maximum angle in transmit, imaging depth and total acquisition time varied depending on the scenario.

1) Stationary acquisition: resolution phantom: To image the wire phantom and measure resolution in a static configuration, 121 plane waves, covering a total sector angle of 60^o (from -30^o to 30^o, 0.5^o step), were transmitted. This is a total of 242 transmission events, since only one transducer transmits at each time while both probes simultaneously receive. The imaging depth and total acquisition time for this sequence were 77 mm and 60.5 ms, respectively. The total sector angle between transmitted plane waves was chosen to be approximately the same as the angle defined between the probes, with the goal of filling the gap in the effective aperture obtained by the coherent multi-transducer method [18].

2) Stationary acquisition: contrast phantom: To image the speckle phantom with the anechoic lesion, the transmit sequence was optimised for the standard coherent PW compounding method for a single transducer and achieve equivalence to a conventional focused system with F-number=1.75

[6], [26]. This results in 41 plane waves for the full angle sequence (total sector 20^o, from -10^o to 10^o, 0.5^o step), per each transducer and in total 82 transmission events for the coherent multi-transducer system. The imaging depth was 77 mm and the total acquisition time 20.5 ms.

3) Free-hand demonstration: During the free-hand demonstration, 21 plane angles (from -5^o to 5^o with a 0.5^o step) were transmitted from each probe and the backscattered signals from up to 55 mm deep were acquired. The total acquisition time using this sequence was 2 s, meaning 4000 frames of data from the pair of transducers (8000 transmit events in total). Data was acquired only from the wire target phantom. In this case, the maximum angle of the emitted plane wave was limited to keep the common FoV of both transducers over time while the probes were moving.

D. Data processing

Optimization was done in Matlab using the simplex search method described in [21]. The initial estimate of the parameters, $\theta_0 = \{c, Q_1, \ldots, Q_K, \phi_1, O_1, \phi_2, O_2\}$, needed to start the optimization algorithm was chosen as follows. Considering the world coordinate system the same as the local coordinate system of transducer T_1 ($\phi_1 = 0,\ O_1 = [0, 0]$), the parameter $\{\phi_2, O_2\}$ that define the position of transducer T_2 were calculated using point-based image registration [27]. Two single images, T_1R_1 and T_2R_2, acquired by each of the transducers were used. For the scatterer positions Q_k and speed of sound of the propagation medium c, an initial value was calculated from the RF data T_1R_1 using the best-fit one-way geometric delay for the echoes returning from the targets, as described in [22].

Optimization was done using all the point-like targets within the shared FoV. For the static experiment, since there is no motion, only one set of optimal parameters is needed and all RF data corresponding to plane waves transmitted at different angles can be beamformed using the same optimal parameters. However, to validate the optimization algorithm, 121 optimal parameter sets were calculated, one per transmit angle and using the same initial estimate. On the other hand, for the free-hand demonstration, each frame was generated using a different set of optimal parameters, where after initializing the algorithm as described above, each subsequent optimization was initialized with the optimum value of the previous frame.

The proposed coherent multi-transducer method was compared with the image acquired using one single transducer and with the incoherent compounding of the envelope-detected images acquired by two independent transducers. The images acquired during the static experiment were used for this image performance analysis. A fully coherent image was obtained using equation (5), by coherently adding the totality of the RF data acquired in one sequence (T_1R_1, T_1R_2, T_2R_1, T_2R_2):

$$S(Q_k; \mathcal{P}_a) = s_{1,1}(Q_k; \mathcal{P}_a^1) + s_{1,2}(Q_k; \mathcal{P}_a^1) + s_{2,1}(Q_k; \mathcal{P}_a^2) + s_{2,2}(Q_k; \mathcal{P}_a^2) \tag{14}$$

Spatial resolution was calculated from the PSF on a single scatterer. An axial-lateral plane for 2-D PSF analysis was chosen by finding the location of the peak value in the elevation dimension from the envelope-detected data. Lateral and axial PSF profiles were taken from the center of the point target. The lateral and axial resolutions were then assessed by measuring the width and the axial (depth) of the PSF at the -6dB level, respectively. In addition, resolution was described using a frequency domain or k-space representation. Axial-lateral RF PSFs were extracted from the beamformed data and the k-space representation was calculated using a 2-D Fourier transform. While the axial resolution is determined by the transmitted pulse length and the transmit aperture function, the lateral response of the system can be predicted by the convolution of the transmit and receive aperture functions [28].

For the anechoic lesion phantom, the contrast and contrast-to-noise ratio (CNR) were measured from the envelope-detected images. Contrast was calculated as,

$$\text{Contrast} = 20 \log_{10}(\mu_i / \mu_o) \tag{15}$$

and CNR was computed as

$$\text{CNR} = \mid \mu_i - \mu_o \mid / \sqrt{\sigma_i^2 + \sigma_o^2} \tag{16}$$

where μ_i and μ_o are the means of the signal inside and outside of the region, respectively, and σ_i and σ_o represent the standard deviation of the signal inside and outside of the region, respectively.

IV. Results

The 121 optimal parameter sets calculated for each of the transmit angles in the static experiment converged to the same solution. For the algorithm initialization, the estimated time from reconstructing the 2 images independently acquired by each probe, running the semi-automated registration method and optimizing the solution was less than 1 minute. Fig. 4 shows the corresponding coherent multi-transducer images obtained using the initial estimate of the parameters and their optimum values. It is clearly shown that the blurring of the PSF presented in the image obtained using the initial estimate of the parameters is reduced after optimization.

The convergence of the method was also validated in the free-hand experiment. In this case, each transmit angle was optimized over the total acquisition time. After calculating the initial estimate of the parameters of the first transmit PW as described in the previous section, each optimization was initialized with the optimum value of the previous transmission event. As expected, rotation and translation parameters changed over acquisition time (following the operator movements), while the speed of sound can be considered constant. The averaged value and the standard deviation of the optimal speed of sound over the acquisition time was 1466.00 m/s $\pm$ 0.66 m/s. The resulting video, showing the sequence of succesfully optimized frames, can be found in the supporting material. [1]

Fig. 5 shows images for the wire phantom obtained using a single transducer (using the RF data T_1R_1 and noted as

[1]This paper has supplementary downloadable material available at http://ieeexplore.ieee.org, provided by the authors. This includes three multimedia AVI format movie clips, which show the results of the free-hand experiments.

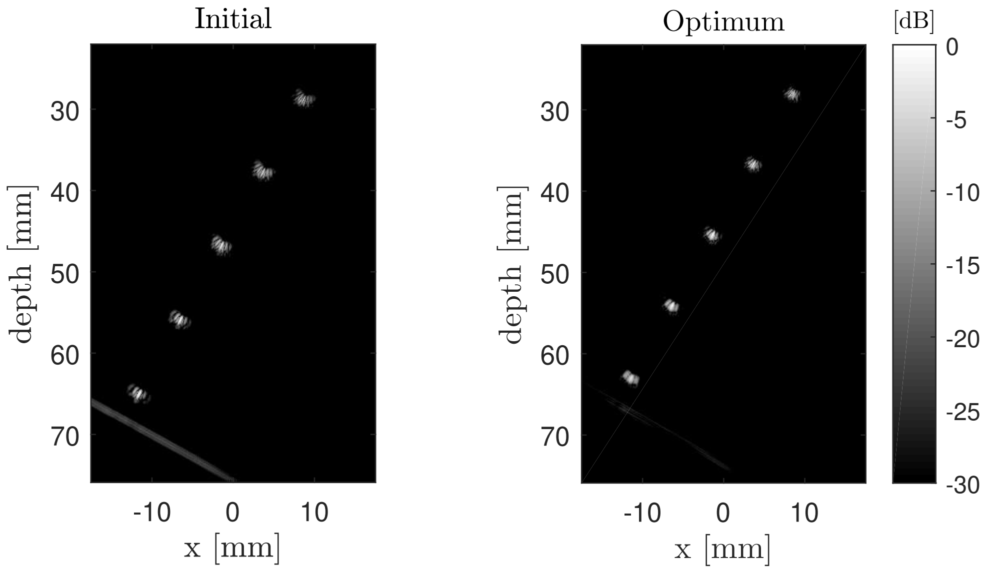

Fig. 4. Experimental coherent multi-transducer images obtained using the initial estimate of the parameters ($\phi_2 = 55.33^o, O_2 = [39.55, 22.83]$ mm, $c = 1496$ m/s) and their optimum values ($\phi_2 = 56.73^o, O_2 = [38.80, 23.06]$ mm, $c = 1450.4$ m/s). Images formed compounding 121 angles over a total angle range of 60^o. Local coordinate system of transducer 1 used as world coordinate system for all images.

Single T1R1), incoherently compounding the images acquired by both transducers (using the envelope-detected images T_1R_1, T_2R_2 and noted as Multi Incoherent) and coherently reconstructing the total RF data (using equation (6) and noted as Multi Coherent) after optimization. Comparing the resulting images between the case with a single transducer and the multi-transducer method, it is observed that the reconstructed images of the wire targets were clearly improved. The PSF of the three images were compared. Fig. 6 and 7 show the corresponding transverse cut of the PSF at the scatterer depth indicated by dotted lines in Fig. 5 for each of these images, using a single PW at 0^o and compounding 121 PW over a total angle range of 60^o, respectively. To analyze the multi-transducer method, the world coordinate system defined at the center of the total aperture, which leads to a more conventional PSF shape where the best resolution is aligned with the x-axis, is used. This coordinate system is defined rotating the local coordinate system of transducer T1 by the bisector angle between the two transducer, as indicated in Fig. 5. Also, note that, the incoherent multi-transducer results shown here benefit from the optimization, as the optimum parameters were used in the incoherent compounding of the enveloped-detected sub-images T_1R_1 and T_2R_2.

The effect of the apodization on the multi-coherent PSF is presented in Fig. 7. The relative performance of all approaches is summarized in Table I. The coherent multi-transducer acquisition presents the best lateral resolution, while the worst one corresponds to the incoherent image generated through combining the independent images acquired by both transducers. Also, larger differences are observed in the behavior of the side lobes, which are higher in the coherent multi-transducer method. When a single PW is used, the biggest difference is between the second side lobes, being raised by 13 dB for the coherent multi-transducer method compared to the single transducer method, while the difference of the first side lobes is 3.5 dB. This suggests that while significant image improvements can be achieved, the image may suffer from the effects of side lobes. The inclusion of the proposed apodization results in a significant reduction of the first side lobe and resolution improvement of 65% compared to the conventional image acquired by a single transducer. In Fig. 5 there is a noticeable variation in the PSF with increasing depth. This is due to the relative spatial position of the individual transducers and to the direction of the transmitted plane waves which determines the generation of the sidelobes in the reconstructed data.

The PSFs obtained using a single transducer and the coherently combined multi-transducer signals were investigated in k-space representation. Fig. 8 shows the corresponding results using a single PW at 0^o. Images are represented in the local coordinate system of transducer 1. An important consequence of the linear system is that the superposition principle can be applied. As expected, the total k-space representation shows an extended lateral region that corresponds to the sum of the four individual k-spaces that form an image in the coherent multi-transducer method. It worth noting that, since both transducers are identical, they have the same k-space response (identical transmit and receive aperture functions) but in different k-space locations. The discontinuity in the aperture of the system, given by the separation between both transducers, leads to gaps in the spatial frequency space. This discontinuity can be filled by compounding PW over an angle range similar to the angle between by the two transducers. Since the lateral extent of k-space that can be reached with steered waves from a single transducer should be double that of the single plane wave (rectangle vs triangle function). Fig. 9 shows the resulting PSF after compounding 121 angles with a separation of 0.5^o, which define a total sector of 60^o, and the corresponding continuous k-space. In addition, the topography of the continuous k-space can be re-shaped

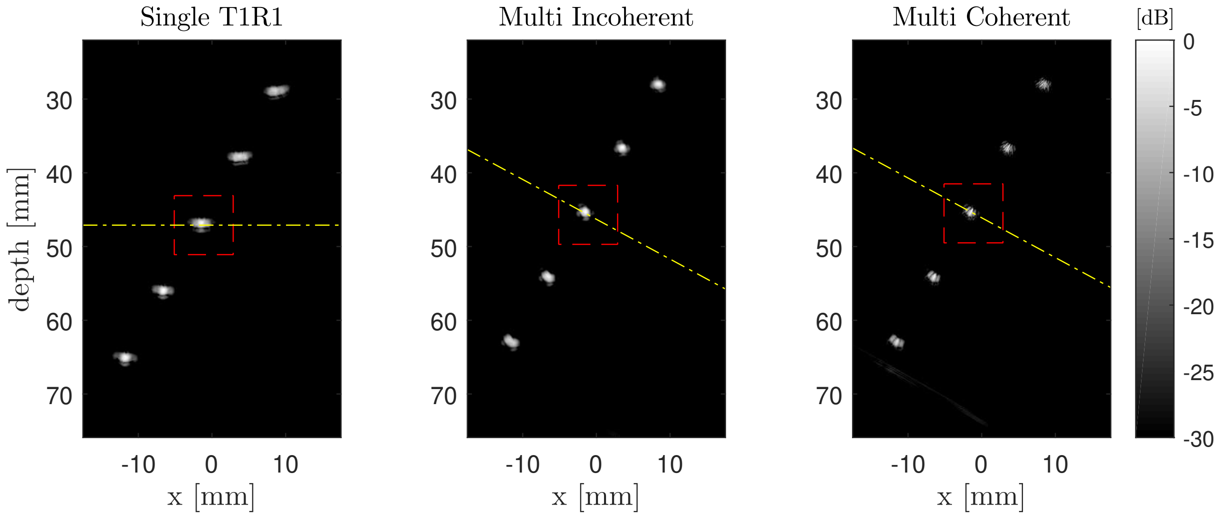

Fig. 5. Experimental images of the wire phantom produced with a single transducer (using the RF data T_1R_1 and noted as Single T1R1), incoherently compounding the images acquired by both transducers (using the envelope-detected images T_1R_1, T_2R_2 and noted as Multi Incoherent) and coherently reconstructing the total RF data (using equation (6) and noted as Multi Coherent). Images formed compounding 121 angles over a total angle range of 60^o. Local coordinate system of transducer 1 used as world coordinate system for all images. PSF and transverse cut at the scatterer depth to estimate resolution are indicated with dashed lines. Note that, PSF and its cross section are calculated in the world coordinate system that leads to the best resolution in each case, i.e., conventional PSF of a single transducer calculated in the local coordinate system of transducer 1, and rotated by the bisector angle between transducers for the others PSFs.

TABLE I
IMAGING PERFORMANCE FOR THE DIFFERENT METHODS ASSESSED USING THE RESOLUTION PHANTOM.

	Axial resolution [mm]	Lateral resolution [mm]	1^{st} sidelobe [dB]	2^{nd} sidelobe [dB]
PW Conventional (1 PW at 0^o)	0.9445	0.6674	-14.96	-20.79
Multi Incoherent (1 PW at 0^o)	0.9474	0.7837	-20.87	-
Multi Coherent (1 PW at 0^o)	0.8109	0.1817	-11.46	-7.01

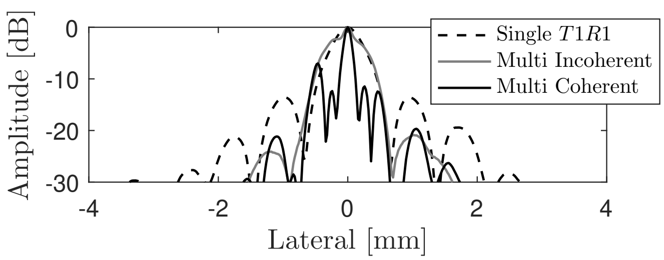

Fig. 6. Transverse cut of the PSF at the scatterer depth defined in Fig. 5 for the single transducer, incoherent and coherent multi-transducer methods. PSFs calculated in the world coordinate system that leads to the best resolution in each case, i.e., conventional PSF of a single transducer calculated in the local coordinate system of transducer 1, and rotated by the bisector angle between transducers for the others PSFs. For comparison, main lobes of the resulting transverse cuts are aligned within the lateral axis. Images formed transmitting a single plane wave at 0^o.

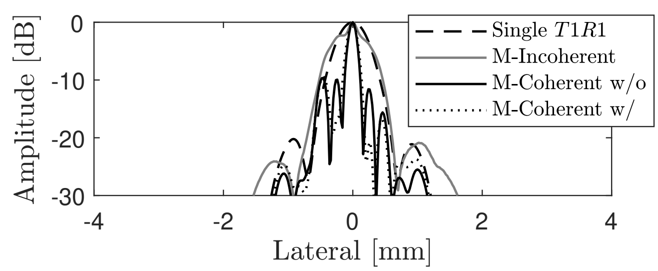

Fig. 7. Transverse cut of the PSF at the scatterer depth defined in Fig. 5 for the single transducer method and coherent multi-transducer method, with (w) and without (w/o) apodization. PSFs calculated in the world coordinate system that leads to the best resolution in each case, i.e., conventional PSF of a single transducer calculated in the local coordinate system of transducer 1, and rotated by the bisector angle between transducers for the others PSFs. For comparison, main lobes of the resulting transverse cuts are aligned within the lateral axis. Images formed compounding 121 plane waves over a total angle range of 60^o.

weighting the data from the different images that are combined to form the total one. A more conventional transfer function with reduced side lobes can be created accentuating the low lateral spatial frequencies, which are mostly defined by the sub-images T_1R_2 and T_2R_1. Using this approach, Fig. 9 shows a PSF and its corresponding k-space representation generated weighting the sub-images T_1R_1, T_1R_2, T_2R_1 and T_2R_2 with the vector $[1, 2, 2, 1]$. Corresponding transverse cut of the PSF and imaging metrics are shown in Fig. 7 and Table I.

The results obtained from the anechoic lesion phantom are presented in Fig. 10 and 11, where the FoV of each transducer is indicated by blue and red lines (T1 and T2 respectively). Fig. 10 shows the individual sub-images that form the final multi coherent image and that are obtained through beamforming the 4 RF datasets acquired in a single cycle of the imaging process, i.e. transmitting a PW at 0^o with probe T1 and simultaneously receiving with both probes (T1R1,T1R2) and repeating the transmission with probe T2 (T2R1,T2R2). Note that, the reconstruction of these sub-images is only possible

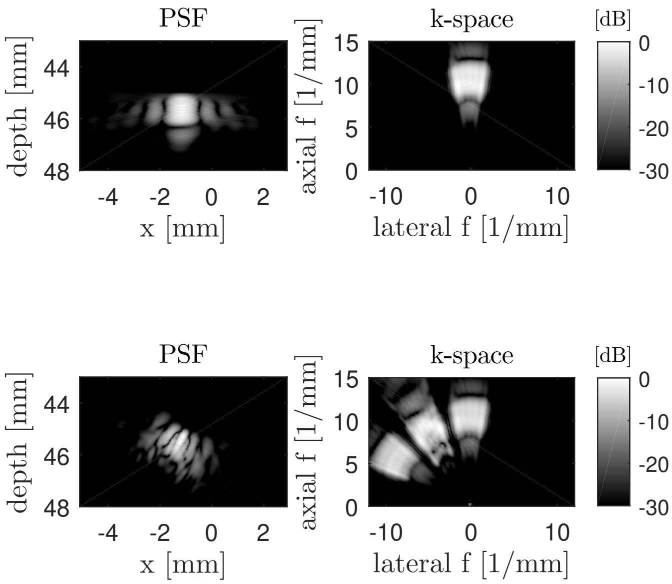

Fig. 8. Envelope-detected PSFs and k-space representation obtained using a single transducer (upper graph) and using the coherent multi-transducer method (bottom graph). Images formed using a single PW at 0^o. Local coordinate system of transducer 1 used as world coordinate system.

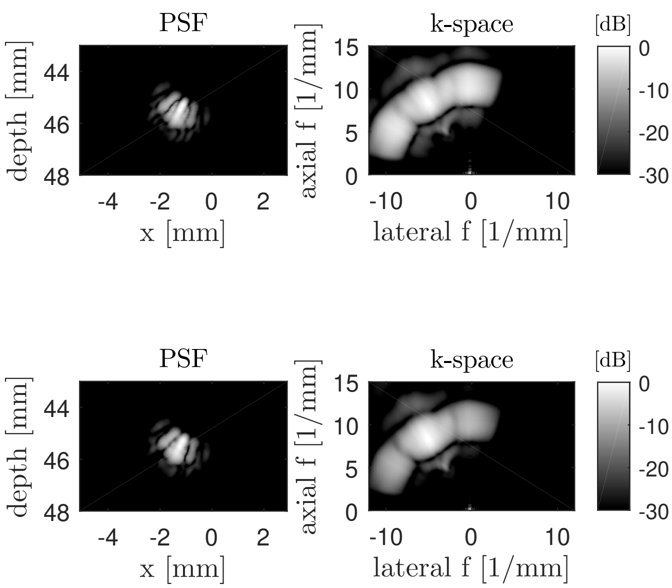

Fig. 9. Envelope-detected PSFs and k-space representation of the multi-transducer method, compounding 121 plane waves covering a total angle range of 60^o, without (upper graph) and with apodization (bottom graph). Local coordinate system of transducer 1 used as world coordinate system.

after finding, through optimization, the relative position of the probes. A direct result of the combination of these 4 sub-images is the extended FoV of the multi coherent image. Fig. 11-c shows the multi coherent image obtained by coherently compounding these 4 sub-images. It can be seen that, as predicted by the k-space representation, any overlapping regions in these sub-images will contribute to improved resolution in the final multi coherent image because of the effective enlarged aperture created.

Images acquired using coherent PW compounding with a single transducer (T_1R_1 and T_2R_2, compounding 41 PW angles) and coherently compounding the RF data acquired by both transducers (using equation (6)) transmitting each one a single PW at 0^o and transmitting each one 41 PW are compared in Fig. 11. Table II shows the corresponding imaging metrics in terms of lateral resolution, contrast, CNR and frame rate. To reconstruct the coherent multi-transducer images, the initial estimate of the parameters was chosen as described in Section III-D and the 3 strong scatterers generated by the nylon wires were used in the optimization. It can be seen that, in general, the multi coherent image has better defined edges, making the border easier to delineate than in the image obtained by a single transducer. The reconstructed images of the wire targets are clearly improved, the speckle size is reduced and the anechoic region is easily identifiable from the phantom background. Resolution significantly improved in the coherent multi-transducer method without frame rate sacrifice and at small expense of contrast. For single transducer, with coherent compounding, the lateral resolution, measured at the first target position is, 1.555 mm (measured at a frame rate of 260 Hz). Using multi-probe image (without additional compounding) the resolution improved to 0.713 mm (with an improved frame rate of 5350 Hz). In the single transducer case, the lesion is visible with a contrast of -8.26 dB and a CNR of 0.795, while both metrics are slightly reduced in the multi-transducer coherent image (without additional compounding) to -7.251 dB and 0.721, respectively. Using compounding with 41 PW over each probe these improve to -8.608 dB and 0.793. These results suggest that target detectability is a function of both resolution and contrast.

The dependence of the imaging depth on the angle between both probes was also investigated. Fig. 12 shows a spatial representation of the FoV of two linear arrays and the depth of the common FoV, measured at the intersection of the center of both individual field of view. The depth of common FoV as function of the angle between both probes when transmitting plane waves at 0^o is described. It can be seen that imaging depth increases at larger angle between the probes.

V. Discussion

This study introduces a new coherent multi-transducer ultrasound system that significantly outperforms single transducer through coherent combination of signals acquired by different synchronized transducers that have a shared FoV. Although the experiments presented here were performed as a demonstration in 2-D using linear arrays, the framework that we propose clearly encompasses the 3rd spatial dimension. In future work the use of matrix arrays capable of volumetric acquisitions could be used for a true 3-D demonstration. Since the multi coherent image is formed by 4 RF datasets that are acquired in two consecutive transmissions, it is necessary that tissue and/or probe motion do not break the coherence between

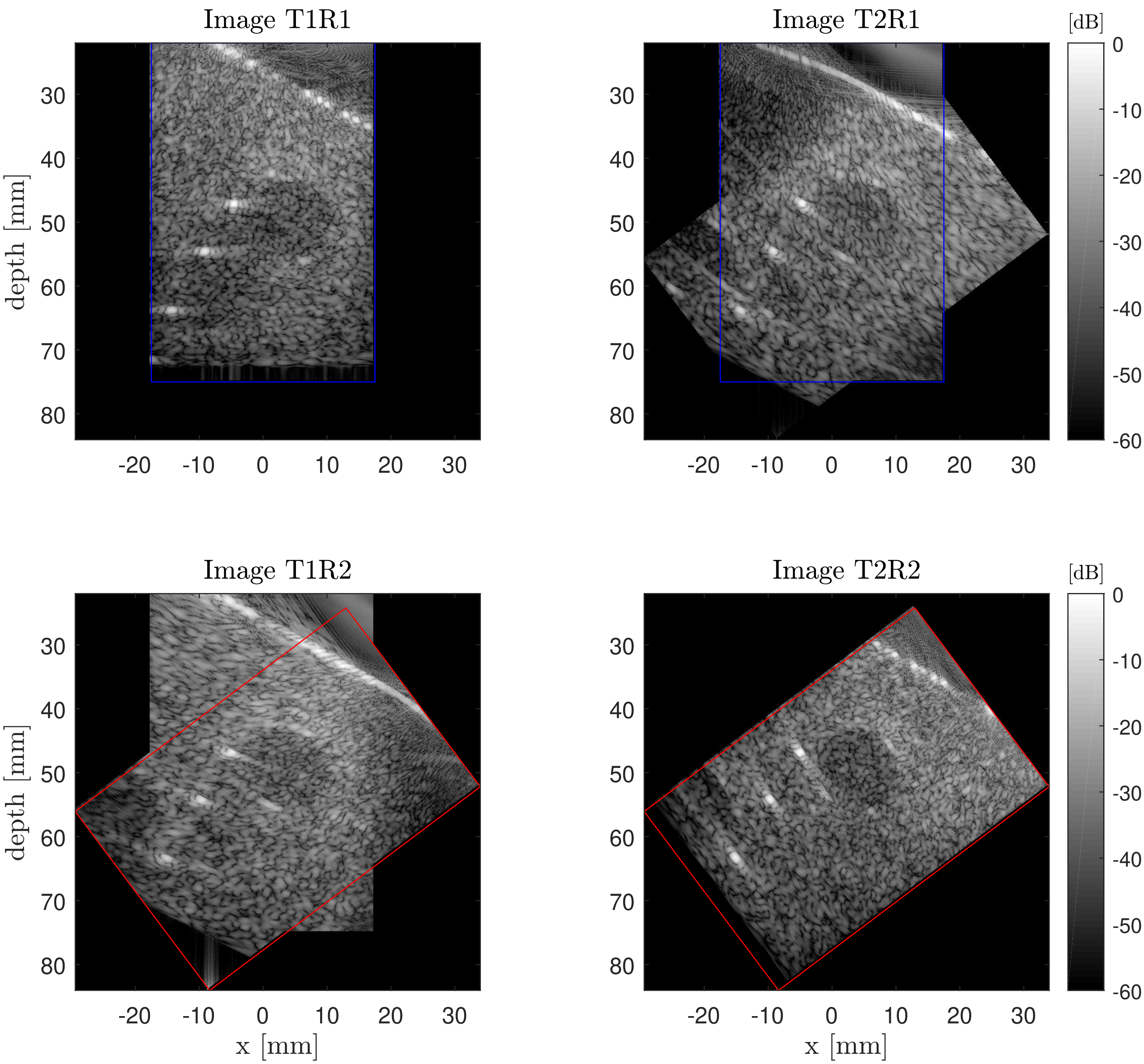

Fig. 10. Individual sub-images that form the final multi coherent image. These were obtained by individually beamforming the 4 RF datasets acquired from one complete sequence, i.e. transmitting a PW at 0^o with probe T_1 and simultaneously receiving with both probes ($\mathrm{T}_1\mathrm{R}_1$,$\mathrm{T}_1\mathrm{R}_2$) and repeating the transmission with probe T_2 ($\mathrm{T}_2\mathrm{R}_1$,$\mathrm{T}_2\mathrm{R}_2$). The optimum parameters used to reconstruct the images are $\phi_2 = 53.05^o, O_2 = [41.10, 25.00]$ mm, $c = 1437.3$ m/s.Lines indicate the field of view of transducer T1 (blue) and T2 (red).

TABLE II
IMAGING PERFORMANCE FOR THE DIFFERENT METHODS ASSESSED USING THE CONTRAST PHANTOM.

	Lateral resolution [mm]	Contrast [dB]	CNR [-]	Frame rate [Hz]
Single T1R1 (1 PW at 0^o)	2.633	-6.708	0.702	10700
Single T1R1 Compounding (41 PW, sector 20^o)	1.555	-8.260	0.795	260
Multi Coherent (1 PW at 0^o)	0.713	-7.251	0.721	5350
Multi Coherent Compounding (41 PW per array, sector 20^o)	0.693	-8.608	0.793	130

consecutive acquisitions. To ensure this is the case high frame rate acquisition is essential. Its performance has been demonstrated using plane waves. However, different transmit beam profiles such as diverging waves may increase the overlapped FoV, extending the final high resolution image. Indeed there is a complex interplay between FoV and resolution gain as probes are moved relative to one another. In the method presented there must be overlap of insonated regions to allow the relative probe positions to be determined. Any overlap in either transmit or receive sensitivity fields will contribute

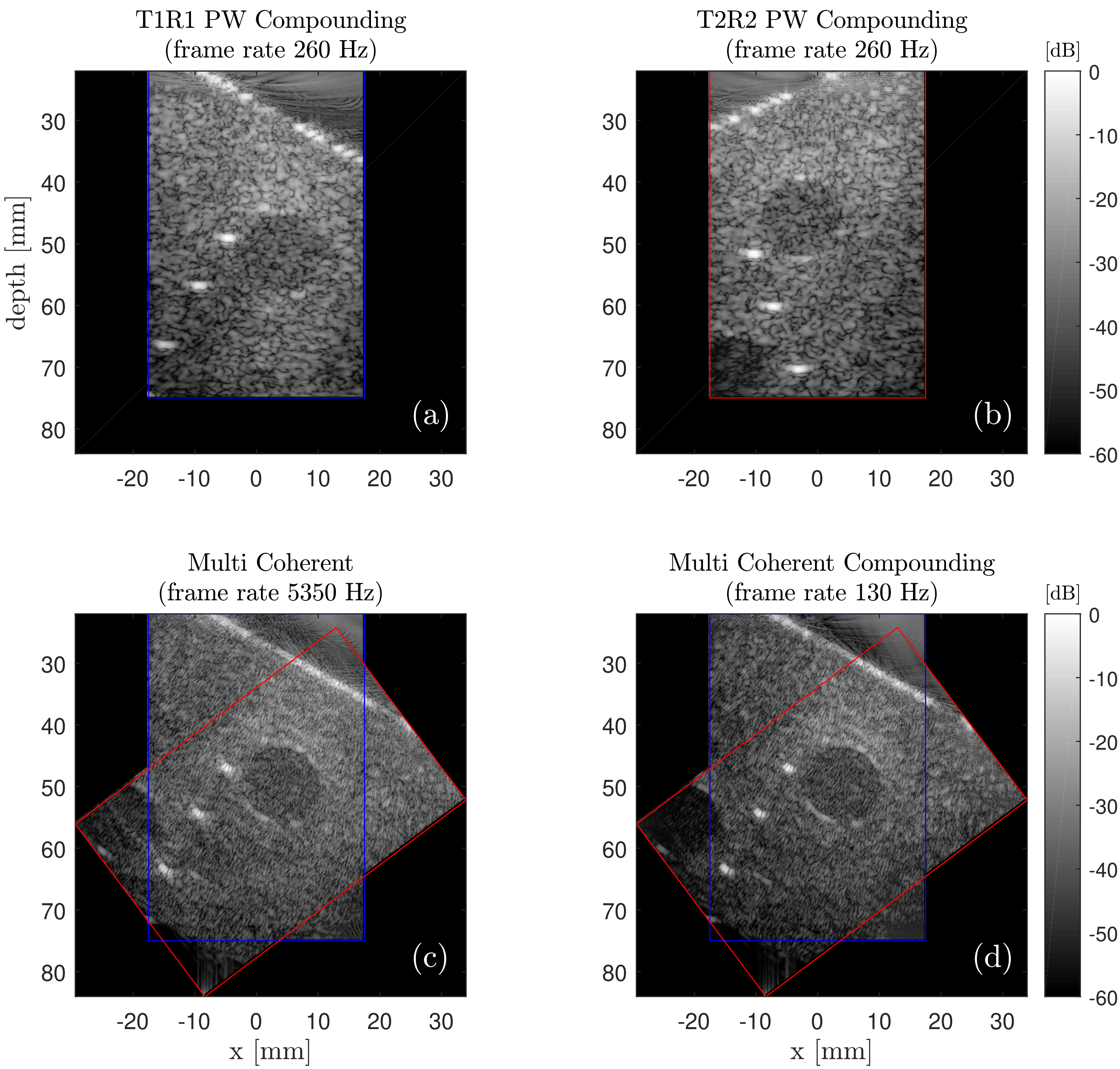

Fig. 11. Experimental images of the contrast phantom obtained by different methods. (a) Coherent plane wave compounding 41 PW with transducer T_1; (b) Coherent plane wave compounding 41 PW with transducer T_2; (c) Coherent multi transducer method with transmission of a single PW at 0^o from each transducer; (d) Coherent multi transducer method with additional compounding and each transducer emitting 41 PW. The optimum parameters used to reconstruct the multi-coherent images are $\phi_2 = 53.05^o, O_2 = [41.10, 25.00]$ mm, $c = 1437.3$ m/s. Lines indicate the field of view of transducer T1 (blue) and T2 (red).

to improved resolution because of the enlarged aperture of the combination of transducers. The final image will always achieve an extended FoV, but the resolution will only improve in regions of overlapping fields. This will be best towards the centre where the overlap includes transmission and receipt for both individual probes. There is also an improvement (albeit lesser) in regions where the overlap is only on transmit or receive fields (see Fig. 10 and 11). Thus there are net benefits, but of different kinds in different locations. In a similar way, this also will determine the imaging depth achieved by the method. While the relative position of the individual transducers and the angles of the transmitted plane waves will determine the depth of the common FoV (see Fig. 12), an improvement of imaging sensitivity in deep regions is expected because the effective receive aperture is larger than in a single probe system.

Our results suggest that the improvements in resolution are mainly determined by the achieved extended aperture rather than compounding PW at different angles. Preliminary simulation results showed that in the coherent multi-transducer

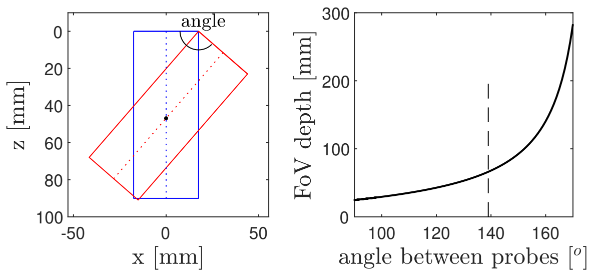

Fig. 12. Schematic representation of the common field of view (FoV) of two probes, T1 (blue) and T2 (red). Depth of common field of view as function of the angle between both probes when transmitting plane waves at 0^o. The dashed line shows the angle and corresponding depth of the configuration shown in the schematic representation. The depth of the FoV is measured at the intersection of the center of both individual field of view.

method there is a trade-off of between resolution and contrast [18]. While a large gap between the probes will result in an extended aperture which improves resolution, the contrast may be compromised due to the effects of sidelobes associated with creation of a discontinuous aperture. Also, additional off-axis scattering may contribute to the side lobe amplitude (see Table I). Further coherent compounding can be used to improve the contrast by reducing sidelobes. Fig. 11 shows that target detectability is determined by both resolution and contrast [29]. The differences between the k-space representations for the single and the coherent multi-transducer methods further explain the differences in imaging performance; the more extended the k-space representation, the higher the resolution [30]. The relative amplitudes of the spatial frequencies present, i.e. the topography of k-space, determine the texture of imaged targets. Weighting the individual data from the different transducers can reshape the k-space, accentuating certain spatial frequencies and so can potentially create a more conventional response for the system. Moreover, the presence of uniformly spaced unfilled areas in a system's k-space response may indicate the presence of grating lobes in the system's spatial impulse response [28]. A sparse array (like our multi-transducer method) creates gaps in the k-space response. Only with minimal separation between transducers the k-space magnitude response will become smooth and continuous over an extended region. This suggests that there is an interplay between the relative spatial positioning of the individual transducers and the angles of the transmitted plane waves; where either one or both of these can determine the resolution and contrast achievable in the final image [18]. There is an opportunity to use the relative position data to decide what range of PW angles to use and to change these on the fly to adaptively change performance. Finally, in real life applications, resolution and contrast will be influenced by a complex combination of probe separation and angle, aperture width, fired PW angle and imaging depth. In the future, we will focus on further investigating these different factors that determine the image performance of the system, including the use of advance beamforming methods [5].

Image enhancements related to increasing aperture size are well described [12]. Nevertheless, in clinical practice the aperture is limited because extending it often implies increasing the cost and the system complexity. This work uses conventional equipment and image-based calibration to extend the effective aperture size while increasing the received amount of RF data (data x N). The estimated time for the first initialization is less than 1 minute, which is comparable to other calibration methods [31], [32]. Once the algorithm has been correctly initialized, the subsequent running times for the optimization can be significantly decreased. For example, in the free-hand experiment, where each optimization was initialized with the output from the previous acquisition, the optimization was up to 4 times faster than the first one. Regarding to the amount of data, similar to 3-D and 4-D ultrafast imaging where the data is significantly large [33], in the proposed multi-transducer method computation may be a bottleneck for real time imaging. Graphical processing unit (GPU)-based platforms and high-speed buses are key to future implementation of these new imaging modes [34]. In addition to the system complexity, large-aperture arrays represents ergonomic operator problems and have limited flexibility to adapt to different applications. In this work, the extended aperture is the result of adding multiple freely placed transducers together, which allows more flexibility. Small arrays are easy to couple to the skin and adapt to the body shape. Notwithstanding, in relation to current ultrasound imaging systems, the use of multiple probes will potentially increase the operational difficulty for the individual performing the scan. However, it is possible to manipulate multiple probes using a single, potentially adjustable, multi-probe holder that would allow the operator to hold multiple probes with only one hand while keeping directed to the same region of interest. In related work, such a probe holder has been demonstrated as a potential device for incoherent combination of multiple images for extended FoV imaging [4]. The approach presented in this study could lead to a totally different strategy in US in which large assemblies of individual arrays are operated coherently together.

To successfully improve the PSF, the proposed multi-transducer method requires coherent alignment of the backscattered echoes from multiple transmit and receive positions. This requirement is only achieved through precise knowledge of all the transducer positions, which in practice is not achievable by manual measurements or using electromagnetic or optical trackers [35]. This study, presents a method for precise and robust transducer location by maximizing the coherence of backscattered echoes arising from the same point scatterer and received by the same transducer using sequential transmissions from each of the transducers of the system. Similar to free-hand tracked ultrasound for image guide applications [31], [32], spatial calibration is essential to guarantee the performance of the proposed multi-coherent ultrasound method. The use of gradient-descent methods requires an initial estimate of the parameters close enough to the global maximum of the cost function, including the position of the calibration targets. It is then expected an increase in the sensitivity errors away from the targets used for calibration. The distance between maxima, which depends on the NCC and corresponds to the pulse length, dictates this tolerance. This is approximately 1.5 μs (equivalent to 2.19 mm) for the experimental configuration used here. This tolerance value can be realistically achieved through image registration [27]. In practice, in a free-hand situation, and assuming that at some initial instant the registration is accurate, this initial guess can be ensured if the transducers move relatively little in the time between two transmissions and share a common FoV. In PW imaging, the frame rate is only limited by the round-trip travel time, which depends on the speed of sound and the depth. For the experimental setup used in this work, the minimum time between two insonifications is around 94 μs. Hence the maximum frame rate is limited to $F_{max} = 10.7$ kHz, which in the case of the present multi transducer coherent method is reduced by the number of probes as F_{max}/N. To guarantee free-hand performance of the multi transducer method, perfect coherent summation must be achieved over consecutive transmissions of the N transducers of the system. However, when the object under insonification moves between transmit events, this condition is no longer achieved. In other words, the free-hand performance is limited by the maximum velocity at which the probes move. Considering that coherence breaks for a velocity at which the observed displacement is larger than half a pulse wavelength per frame [26], the maximum velocity of the probes is $V_{max} = \lambda F_{max}/2N$, which in the example showed here is 1.33 m/s. This speed far exceeds the typical operator hand movements in a regular scanning session and hence, the coherent summation over two consecutive transmission is achieved. The method has been validated in a free-hand demonstration.

Wavefront aberration caused by inhomogeneous medium can significantly limit the quality of medical ultrasound images and is the major barrier to achieve diffraction-limited resolution with large aperture transducers [36]. In the situation where there is no variation in the speed of sound through the medium, the result of the optimisation will remain valid throughout the imaged region. Even in areas distant from the targets used for calibration. However, in the presence of variation in speed of sound, errors in the applicability of the transform are likely to increase in regions further from the targets. The technique described in this work has been tested in a scattering medium, with the assumption of a constant speed of sound along the propagation path. However, since the speed of sound is a parameter in the optimization, the technique could be adapted for nonhomogeneous media where the speed of sound varies in space [18]. In this case, the medium could be modeled through piecewise continuous layers. The optimization method could be applied in a recursive way, dividing the FoV in sub areas with different speeds of sound. More accurate speed of sound estimation would improve beamforming and allow higher order phase aberration correction. Potentially representing speed of sound maps would be of great interest in tissue characterization [37], [38]. In addition, the use of multiple transducers allows multiple interrogations from different angles, which might give insight into the aberration problem and help to test new algorithms to remove the clutter.

Further studies are needed to predict the performance of the proposed multi-transducer system for *in-vivo* imaging. The approach presented here has been formulated and validated for detectable and isolated point scatterers within the shared imaging region, which in practice may not be always possible. However, although the theory was presented for point-like scatterers, the approach relies on a measure of coherence which may well be more tolerant, as indicated in the contrast phantom demonstrated in Fig. 11. This result suggests that the method may work when there are identifiable prominent local features, and the concept of maximizing coherence of data received by each receiver array when insonated by different transmitters could allow wider usage. Indeed, an optimization based on spatial coherence might be more robust in the case where point targets are not available, due to the expected decorrelation of speckle with receiver location [39]–[41]. This may also lead to improvements in computational efficiency. Measures of spatial coherence have been used previously in applications such as phase aberration correction [42], flow measurements [43], and beamforming [44]. On the other hand, isolated point scatterers can be artificially generated by other techniques, for instance by inclusion of microbubble contrast agents [45]. Recently, ultrasound super-resolution imaging has demonstrated that spatially isolated individual bubbles can be considered as point scatterers in the acoustic field [46] and accurately localized [47]. The feasibility of the coherent multi-transducer method in complex media, including a new approach mainly based on spatial coherence [20], [40] and the potential use of microbubbles will be the focus of future work.

VI. Conclusion

In this study a new coherent multi-transducer ultrasound imaging system and a robust method to accurately localize the multiple transducers have been presented. The subwavelength localization accuracy required to merge information from multiple probes is achieved by optimizing the coherence function of the backscattered echoes coming from the same point scatterer insonated by sequentially all transducers and received by the same one, without the use of an external tracking device. The theory for the approach was general for a multiplicity of 2-D arrays placed in 3-D and the method was experimentally validated in a 2-D framework using a pair of linear array and ultrasound phantoms. The improvements in imaging quality have been shown. Overall the performance of the multi-transducer approach is better than plane wave imaging with one single linear array, enhancing resolution and extending the field of view while keeping high acquisition frame rates. Results suggest that the coherent multi-transducer imaging has the potential to improve ultrasound image quality in a wide range of scenarios.

Acknowledgment

This work was supported by the Wellcome/EPSRC Centre for Medical Engineering [WT 203148/Z/16/Z] and the Wellcome Trust IEH Award [102431]. The authors acknowledge financial support from the Department of Health via the National Institute for Health Research (NIHR) comprehensive Biomedical Research Centre award to Guy's & St Thomas' NHS Foundation Trust in partnership with King's College London and King's College Hospital NHS Foundation Trust. The views expressed are those of the authors and not necessarily those of the NHS, the NIHR or the Department of Health.

References

[1] M. Klysik, S. Garg, S. Pokharel, J. Meier, N. Patel, and K. Garg, "Challenges of imaging for cancer in patients with diabetes and obesity," *Diabetes technology & therapeutics*, vol. 16, no. 4, pp. 266–274, 2014.

[2] P.-J. S. Tsai, M. Loichinger, and I. Zalud, "Obesity and the challenges of ultrasound fetal abnormality diagnosis," *Best Practice & Research Clinical Obstetrics & Gynaecology*, vol. 29, no. 3, pp. 320–327, 2015.

[3] L. Weng, A. P. Tirumalai, C. M. Lowery, L. F. Nock, D. E. Gustafson, P. Von Behren, and J. H. Kim, "US extended-field-of-view imaging technology." *Radiology*, vol. 203, no. 3, pp. 877–880, 1997.

[4] V. A. Zimmer, A. Gomez, Y. Noh, N. Toussaint, B. Khanal, R. Wright, L. Peralta, M. van Poppel, E. Skelton, J. Matthew, and J. A. Schnabel, "Multi-view image reconstruction: Application to fetal ultrasound compounding," in *Data Driven Treatment Response Assessment and Preterm, Perinatal, and Paediatric Image Analysis*, A. Melbourne, R. Licandro, M. DiFranco, P. Rota, M. Gau, M. Kampel, R. Aughwane, P. Moeskops, E. Schwartz, E. Robinson, and A. Makropoulos, Eds. Cham: Springer International Publishing, 2018, pp. 107–116.

[5] J.-F. Synnevag, A. Austeng, and S. Holm, "Benefits of minimum-variance beamforming in medical ultrasound imaging," *IEEE Transactions on Ultrasonics, Ferroelectrics, and Frequency Control*, vol. 56, no. 9, pp. 1868–1879, 2009.

[6] G. Montaldo, M. Tanter, J. Bercoff, N. Benech, and M. Fink, "Coherent plane-wave compounding for very high frame rate ultrasonography and transient elastography," *IEEE Transactions on Ultrasonics, Ferroelectrics and Frequency Control*, vol. 56, no. 3, pp. 489–506, 3 2009. [Online]. Available: http://ieeexplore.ieee.org/document/4816058/

[7] G. Matrone, A. Ramalli, A. S. Savoia, P. Tortoli, and G. Magenes, "High frame-rate, high resolution ultrasound imaging with multi-line transmission and filtered-delay multiply and sum beamforming," *IEEE Transactions on Medical Imaging*, vol. 36, no. 2, pp. 478–486, 2017.

[8] J. Bercoff, G. Montaldo, T. Loupas, D. Savery, F. Mézière, M. Fink, and M. Tanter, "Ultrafast compound doppler imaging: Providing full blood flow characterization," *IEEE Transactions on Ultrasonics, Ferroelectrics, and Frequency Control*, vol. 58, no. 1, pp. 134–147, 2011.

[9] M. Karaman, P.-C. Li, and M. O'Donnell, "Synthetic aperture imaging for small scale systems," *IEEE Transactions on Ultrasonics, Ferroelectrics, and Frequency Control*, vol. 42, no. 3, pp. 429–442, 1995.

[10] K. L. Gammelmark and J. A. Jensen, "Multielement synthetic transmit aperture imaging using temporal encoding," *IEEE Transactions on Medical Imaging*, vol. 22, no. 4, pp. 552–563, 2003.

[11] M. Moshfeghi and R. Waag, "In vivo and in vitro ultrasound beam distortion measurements of a large aperture and a conventional aperture focussed transducer," *Ultrasound in Medicine and Biology*, vol. 14, no. 5, pp. 415–428, 1988.

[12] N. Bottenus, W. Long, M. Morgan, and G. Trahey, "Evaluation of large-aperture imaging through the ex vivo human abdominal wall," *Ultrasound in Medicine & Biology*, 2017.

[13] H. K. Zhang, A. Cheng, N. Bottenus, X. Guo, G. E. Trahey, and E. M. Boctor, "Synthetic tracked aperture ultrasound imaging: design, simulation, and experimental evaluation," *Journal of Medical Imaging*, vol. 3, no. 2, pp. 027 001–027 001, 2016.

[14] K. L. Gammelmark and J. A. Jensen, "2-D tissue motion compensation of synthetic transmit aperture images," *IEEE Transactions on Ultrasonics, Ferroelectrics, and Frequency Control*, vol. 61, no. 4, pp. 594–610, 2014.

[15] H. K. Zhang, R. Finocchi, K. Apkarian, and E. M. Boctor, "Co-robotic synthetic tracked aperture ultrasound imaging with cross-correlation based dynamic error compensation and virtual fixture control," in *Ultrasonics Symposium (IUS), 2016 IEEE International*. IEEE, 2016, pp. 1–4.

[16] N. Bottenus, W. Long, H. K. Zhang, M. Jakovljevic, D. P. Bradway, E. M. Boctor, and G. E. Trahey, "Feasibility of swept synthetic aperture ultrasound imaging," *IEEE Transactions on Medical Imaging*, vol. 35, no. 7, pp. 1676–1685, 2016.

[17] L. Peralta, A. Gomez, J. V. Rainal, and R. J. Eckersley, "Feasibility study of a coherent multi-transducer US imaging system," in *2018 IEEE International Ultrasonics Symposium (IUS)*. IEEE, 2018, pp. 1–4.

[18] L. Peralta, A. Gomez, J. V. Hajnal, and R. J. Eckersley, "Coherent multi-transducer ultrasound imaging in the presence of aberration," in *Medical Imaging 2019: Ultrasonic Imaging and Tomography*, vol. 10955. International Society for Optics and Photonics, 2019. [Online]. Available: https://doi.org/10.1117/12.2511776

[19] A. W. Fitzgibbon, "Robust registration of 2D and 3D point sets," *Image and Vision Computing*, vol. 21, no. 13-14, pp. 1145–1153, 2003.

[20] R. Mallart and M. Fink, "The van cittert–zernike theorem in pulse echo measurements," *The Journal of the Acoustical Society of America*, vol. 90, no. 5, pp. 2718–2727, 1991.

[21] J. C. Lagarias, J. A. Reeds, M. H. Wright, and P. E. Wright, "Convergence properties of the nelder–mead simplex method in low dimensions," *SIAM Journal on Optimization*, vol. 9, no. 1, pp. 112–147, 1998.

[22] M. E. Anderson and G. E. Trahey, "The direct estimation of sound speed using pulse–echo ultrasound," *The Journal of the Acoustical Society of America*, vol. 104, no. 5, pp. 3099–3106, 1998.

[23] Y. Desailly, O. Couture, M. Fink, and M. Tanter, "Sono-activated ultrasound localization microscopy," *Applied Physics Letters*, vol. 103, no. 17, p. 174107, 2013.

[24] B. T. Fang, "Trilateration and extension to global positioning system navigation," *Journal of Guidance, Control, and Dynamics*, vol. 9, no. 6, pp. 715–717, 1986.

[25] E. Boni, L. Bassi, A. Dallai, F. Guidi, V. Meacci, A. Ramalli, S. Ricci, and P. Tortoli, "ULA-OP 256: A 256-channel open scanner for development and real-time implementation of new ultrasound methods," *IEEE Transactions on Ultrasonics, Ferroelectrics and Frequency Control*, vol. 63, no. 10, pp. 1488–1495, 2016.

[26] B. Denarie, T. A. Tangen, I. K. Ekroll, N. Rolim, H. Torp, T. Bjåstad, and L. Lovstakken, "Coherent plane wave compounding for very high frame rate ultrasonography of rapidly moving targets," *IEEE Transactions on Medical Imaging*, vol. 32, no. 7, pp. 1265–1276, 2013.

[27] R. A. Beasley, J. D. Stefansic, A. J. Herline, L. Guttierez, and R. L. Galloway, "Registration of ultrasound images," in *Medical Imaging 1999: Image Display*, vol. 3658. International Society for Optics and Photonics, 1999, pp. 125–133.

[28] W. F. Walker and G. E. Trahey, "The application of k-space in pulse echo ultrasound," *IEEE Transactions on Ultrasonics, Ferroelectrics and Frequency Control*, vol. 45, no. 3, pp. 541–558, 1998.

[29] S. W. Smith, R. F. Wagner, J. M. Sandrik, and H. Lopez, "Low contrast detectability and contrast/detail analysis in medical ultrasound," *IEEE Transactions on Sonics and Ultrasonics*, vol. 30, no. 3, pp. 164–173, 1983.

[30] M. E. Anderson and G. E. Trahey, "A seminar on k-space applied to medical ultrasound," *Department of Biomedical Engineering, Duke University*, 2000.

[31] M. Najafi, N. Afsham, P. Abolmaesumi, and R. Rohling, "A closed-form differential formulation for ultrasound spatial calibration: multi-wedge phantom," *Ultrasound in Medicine & Biology*, vol. 40, no. 9, pp. 2231–2243, 2014.

[32] E. Boctor, A. Viswanathan, M. Choti, R. H. Taylor, G. Fichtinger, and G. Hager, "A novel closed form solution for ultrasound calibration," in *Biomedical Imaging: Nano to Macro, 2004. IEEE International Symposium on*. IEEE, 2004, pp. 527–530.

[33] J. Provost, C. Papadacci, J. E. Arango, M. Imbault, M. Fink, J.-L. Gennisson, M. Tanter, and M. Pernot, "3D ultrafast ultrasound imaging in vivo," *Physics in Medicine & Biology*, vol. 59, no. 19, p. L1, 2014.

[34] M. Tanter and M. Fink, "Ultrafast imaging in biomedical ultrasound," *IEEE Transactions on Ultrasonics, Ferroelectrics, and Frequency Control*, vol. 61, no. 1, pp. 102–119, 2014.

[35] L. Mercier, T. Langø, F. Lindseth, and L. D. Collins, "A review of calibration techniques for freehand 3-D ultrasound systems," *Ultrasound in Medicine & Biology*, vol. 31, no. 2, pp. 143–165, 2005.

[36] J. C. Lacefield, W. C. Pilkington, and R. C. Waag, "Distributed aberrators for emulation of ultrasonic pulse distortion by abdominal wall," *Acoustics Research Letters Online*, vol. 3, no. 2, pp. 47–52, 2002.

[37] J. Bamber and C. Hill, "Acoustic properties of normal and cancerous human liver-I. dependence on pathological condition," *Ultrasound in Medicine & Biology*, vol. 7, no. 2, pp. 121–133, 1981.

[38] M. Imbault, A. Faccinetto, B.-F. Osmanski, A. Tissier, T. Deffieux, J.-L. Gennisson, V. Vilgrain, and M. Tanter, "Robust sound speed estimation for ultrasound-based hepatic steatosis assessment," *Physics in Medicine and Biology*, vol. 62, no. 9, p. 3582, 2017.

[39] N. Bottenus and K. F. Üstüner, "Acoustic reciprocity of spatial coherence in ultrasound imaging," *IEEE Transactions on Ultrasonics, Ferroelectrics, and Frequency Control*, vol. 62, no. 5, p. 852, 2015.

[40] D.-L. Liu and R. C. Waag, "About the application of the van cittert-zernike theorem in ultrasonic imaging," *IEEE Transactions on Ultrasonics, Ferroelectrics, and Frequency Control*, vol. 42, no. 4, pp. 590–601, 1995.

[41] W. F. Walker and G. E. Trahey, "Speckle coherence and implications for adaptive imaging," *The Journal of the Acoustical Society of America*, vol. 101, no. 4, pp. 1847–1858, 1997.

[42] D.-L. Liu and R. C. Waag, "Estimation and correction of ultrasonic wavefront distortion using pulse-echo data received in a two-dimensional

aperture," *IEEE Transactions on Ultrasonics, Ferroelectrics, and Frequency Control*, vol. 45, no. 2, pp. 473–490, 1998.

[43] Y. L. Li and J. J. Dahl, "Coherent flow power doppler (CFPD): flow detection using spatial coherence beamforming," *IEEE Transactions on Ultrasonics, Ferroelectrics, and Frequency Control*, vol. 62, no. 6, pp. 1022–1035, 2015.

[44] M. A. Lediju, G. E. Trahey, B. C. Byram, and J. J. Dahl, "Short-lag spatial coherence of backscattered echoes: Imaging characteristics," *IEEE Transactions on Ultrasonics, Ferroelectrics, and Frequency Control*, vol. 58, no. 7, 2011.

[45] L. Peralta, K. Christensen-Jeffries, R. Paley, J. V. Hajnal, and R. J. Eckersley, "Microbubble contrast agents for coherent multi-transducer ultrasound imaging," in *The 24st European Symposium on Ultrasound Contrast Imaging*. ICUS, 2019, pp. 96–97.

[46] K. Christensen-Jeffries, R. J. Browning, M.-X. Tang, C. Dunsby, and R. J. Eckersley, "In vivo acoustic super-resolution and super-resolved velocity mapping using microbubbles," *IEEE Transactions on Medical Imaging*, vol. 34, no. 2, pp. 433–440, 2015.

[47] K. Christensen-Jeffries, S. Harput, J. Brown, P. N. Wells, P. Aljabar, C. Dunsby, M.-X. Tang, and R. J. Eckersley, "Microbubble axial localization errors in ultrasound super-resolution imaging," *IEEE Transactions on Ultrasonics, Ferroelectrics, and Frequency Control*, vol. 64, no. 11, pp. 1644–1654, 2017.

Laura Peralta Laura Peralta received the BSc and MSc degrees in civil engineering in 2008, and the MSc degree in structural mechanics and the PhD degree in 2012 and 2015, respectively, from the University of Granada, Granada, Spain. As part of her PhD program, she spent some time at the Institut Langevin, Paris, France and at University College London, London, UK. From 2015 to 2017 she was with the Laboratoire d'Imagerie Biomédicale, Paris, France as postdoctoral researcher, working on quantitative ultrasound bone assessment. She is currently a Research Fellow at the Department of Biomedical Engineering, King's College London, London, UK. Her current research interests include biomedical applications of ultrasound, tissue characterization and ultrasound propagation in complex media.

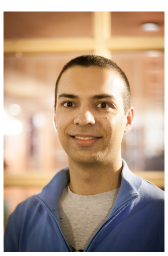

Alberto Gomez Alberto Gomez received his BSc degree in Telecommuncications Engineering from the Technical University of Madrid, Spain, in 2009, and a BSc degree in Telecomminications Engineering and an MRes in image and signal processing from IMT-Atlantique, Brest, France, on the same year. He received his PhD degree from King's College London in 2013. He is currently a Research Fellow at the Department of Biomedical Engineering, King's College London, London, UK. His research interests include ultrasound image acquisition and analysis for cardiac and fetal applications, image visualization and computer vision.

Ying Luan Ying Luan was born in Nanjing, China. She was educated in China, Sweden and the Netherlands where she earned her PhD at Erasmus University Medical Center, Rotterdam. Her areas of expertise are physical acoustics, medical ultrasound, and ultrasound contrast agents for imaging and drug delivery. Ying Luan is currently working as Technology Leader on ultrasound contrast agents at R&D Pharmaceutical diagnostics at GE Healthcare, Amersham, UK. Prior to joining GE, Ying worked as Research Associate at King's College London with a team of scientists and clinicians on developing novel imaging algorithms for intelligent fetus imaging and diagnosis.

Bae-Hyung Kim Bae-Hyung Kim was born in Seoul, Korea in 1976. He received the BSc, MSc and PhD degrees in the Department of Electronic Engineering from Sogang University, Seoul, Korea, in 2001, 2003 and 2007, respectively. From 2007 to 2010, he was a Principal Engineer with Siemens Ultrasound Systems Korea to conduct the research and development of commercialized ultrasound machine. He worked at Samsung Advanced Institute of Technology (SAIT), Samsung Electronics Co. Ltd, Korea, as a research staff member from 2010 through 2015. At SAIT, he was leading the R&D of volumetric ultrasound system for 2-D CMUT-on-ASIC array. After about 9 years' experience in industry, he moved to academia to find a new opportunity. He started a fresh Ph.D. position as a postdoctoral research associate in the Department of Biomedical Engineering of King's College London, UK from 2015 to 2016. He worked in the Department of Physiology and Biomedical Engineering of Mayo Clinic College of Medicine, Rochester, MN, as a Senior Research Fellow from 2016 to 2018. From October 2018, he is working for Vave Health Inc., San Mateo, CA as a Director. Dr. Kim's research areas at Mayo Clinic include ultrasonic methods for tissue viscoelasticity estimation for applications in cancer imaging and bladder function evaluation. As such, he has broader and in-depth experience and knowledge in most of ultrasound imaging and systems area. He holds 43 patents filed including 13 granted patents in ultrasound imaging and system technologies. His R&D area includes the development of novel ultrasonic instrumentation for ultra-simple front-end architecture and novel ultrasonic techniques for imaging soft tissue microstructure, viscoelasticity and blood-flow. He is also interested in the principles of imaging system design and signal processing, detection, and estimation.

Joseph V Hajnal Following his PhD, Professor Hajnal started as Postdoctoral Research Assistant to Professor J F Nye FRS, at Bristol University in 1984, studying spatial relationships between singularities in the electric and magnetic fields of monochromatic electromagnetic waves. From 1986 to 1989, he worked at Melbourne University as Postdoctoral Research Fellow, School of Physics, and the Laser Physics Centre Australian National University working with Professor G I Opat, devising and conducting experiments in the field of de Broglie Wave Optics. From 1990 to 1997, he worked as Research Scientist at the Picker Research Group, GEC Hirst Research Centre. Attached to the NMR Unit, Hammersmith Hospital, he conducted research into bio-medical applications of NMR with particular emphasis on extending the range of physical phenomena and techniques that can be exploited for radiological and scientific purposes. From 1992, Prof. Hajnal was also an Honorary Lecturer and Senior Lecturer at the Royal Postgraduate Medical School, Hammersmith Hospital. Prof. Hajnal was appointed Professor of Imaging Sciences in 2002, Group Head for MRC Clinical Sciences Centre, Imperial College of Science in 2005 and in 2006 he was made Head of Department, Imaging Sciences Department, Division Clinical Sciences, Faculty of Medicine, Imperial College of Science, Technology and Medicine. In 2012 he joined King's College London as a Chair in Imaging Sciences. In 2014 Professor Hajnal became a Fellow of the International Society of Magnetic Resonance in Medicine.

Robert J. Eckersley Robert J. Eckersley received the BSc degree in physics from Kings College London, London, UK, in 1991, and the PhD degree from the University of London, London, in 1997, while studying at the Institute of Cancer Research, Royal Marsden Hospital, London. He was with the Hammersmith Hospital NHS Trust, London, and in 1999 was awarded a MRC Research Training fellowship. As part of this fellowship, he spent some time at the University of Toronto at the Sunnybrook Health Sciences Centre, Toronto, ON, Canada. He subsequently continued as a Post-Doctoral researcher within the Imaging Sciences Department, Imperial College London, London, and became a nonclinical Lecturer in Ultrasound in 2007. In 2012, he joined the Biomedical Engineering Department, Kings College London, as a Senior Lecturer. His research interests range from fundamental studies to clinical applications, including image and signal analysis of ultrasound data for functional imaging or tissue characterization, nonlinear imaging for improved detection of microbubbles, and understanding errors and artifacts in ultrasound contrast imaging.